Robust Sliding-Mode Control Design for a Voltage Regulated Quadratic Boost Converter

Oswaldo Lopez-Santos*, *Student Member, IEEE,* Luis Martinez-Salamero, *Senior Member, IEEE,* Germain Garcia, Hugo Valderrama-Blavi, *Member, IEEE,* and Tomás Sierra-Polanco

Abstract

A robust controller design to obtain output voltage regulation in a quadratic boost converter with high DC-gain is discussed in this paper. The proposed controller has an inner loop based on sliding-mode control whose sliding surface is defined for the input inductor current. The current reference value of the sliding surface is modified by a proportional-integral (PI) compensator in an outer loop which operates over the output voltage error. The stability of the two-loop controller is proved by using the Routh-Hurwitz criterion, which determines a region in the K_p- K_i plane where the closed-loop system is always stable. The analysis of the sliding mode-based control loop is performed by means of the equivalent control method while the outer loop compensator is derived by means of the Nyquist- based Robust Loop Shaping approach with the M-constrained Integral Gain Maximization technique (RLS-MIGO). Robustness is analyzed in depth taking into account the parameter variation related with the operation of the converter in different equilibrium points. Simulations and experimental results are presented to validate the approach for a 20 - 100 W quadratic boost converter stepping-up a low DC voltage (15 – 25 V DC) to a 400 V DC level.

This work was supported in part by the Spanish Ministerio de Ciencia e Innovación under the projects DPI 2012-31580 and CSD 2009-00046, and the Universidad de Ibagué under project 12-259-COL0007284.

O. Lopez-Santos is with the Electronics Engineering Department, Universidad de Ibagué, Colombia, also with the LAAS-CNRS Univ de Toulouse, France, and also with INSA Univ de Toulouse, France.

G. Garcia is with the LAAS-CNRS Univ de Toulouse, France and also with INSA Univ de Toulouse, France.

L. Martinez-Salamero and H. Valderrama-Blavi are with the Departament d'Enginyeria Electrònica, Elèctrica I Automàtica, Escola Tècnica Superior d'Enginyeria, Universitat Rovira I Virgili, Tarragona 43007, Spain.

T. Sierra-Polanco is with the Natural Science and Mathematics Department, Universidad de Ibagué, Colombia.

*Corresponding author. Email: oswaldo.lopez@unibague.edu.co. Postal Address: Carrera 22 Calle 67 Barrio Ambalá, Ibagué, Colombia. Telephone number (+57) 8 2709400 Ext: 268.

Index Terms

Quadratic boost converter, robust loop shaping, sliding-mode control.

I. INTRODUCTION

THE NEED OF DEVELOPING ad-hoc electronic equipment for power distributed systems, electric vehicles and energy backup architectures, which are supplied by batteries, fuel-cells, photovoltaic modules or other DC sources [1]-[3], is prompting engineers to use a 400 V DC bus as a core of the distribution. Examples of this are residential micro-grids, hybrid vehicles, telecom installations and data centers among others [4]-[5]. As a consequence, non-standard DC-DC converters with the capability to step-up a low DC voltage to a high-voltage level are required since the canonical boost converter has severe constraints to obtain gains higher than ten [6]. Although both transformer-based and transformer-less topologies can be proposed, the requirements in power density, weight, size and cost of the new devices make the transformer-less topologies a more interesting choice [7]-[10]. Among these topologies, single-switch converters derived of the conventional boost converter, such as quadratic boost and the cubic boost converters can be attractive solutions since they can operate within a safe duty cycle range avoiding modulator saturation [11]. Besides, the quadratic boost converter shows a better trade-off between efficiency and duty cycle operating range than the cubic boost converter because of the higher complexity and number of components of the cubic structure [12].

Moreover, robust control of the boost converter has become an attractive research field in the last years due to the non-minimum phase nature of its control to output transfer function, which results from the linearization of the converter averaged equations around the steady-state and whose parameters have a high degree of uncertainty. To solve this problem, different methods have been proposed such as robust gain scheduled control [13], robust LQR control [14], robust non-linear adaptive control [15] and internal mode control [16], among others. Although the quadratic boost converter is a boost- derived converter topology, its structure has a higher complexity and so far few solutions have been reported, all existing proposals being based on pulse width modulation. The first approaches were based on cascade control with an inner current loop which is obtained using average current control [17] or current programmed control [18], and an outer voltage loop which regulates the output voltage using a PI compensator whose design does not consider the uncertainty in the converter parameters. A more recent proposal uses the

same scheme to regulate the output voltage of the quadratic boost converter, but tackles the control problem using reduced redundant power processing (RRPP) [19]. In addition, a theoretical approach solving the control problem by means of a linear combination of the states instead of using a cascade type multi-loop control has been recently presented in [20], but its electronic implementation would be considerably complex. Besides, another approach using an adaptive PI regulator has been presented in [21] where the main goal has been proving the stability from an incremental passivity perspective, but without presenting experimental results validating the approach. Hence, designing a robust controller for voltage regulation in a quadratic boost converter is still an open problem whose solution can help engineers to better exploit this converter in transformer-less high DC gain applications.

The aim of this paper is to tackle the problem of regulating the output voltage in the quadratic boost converter operating in continuous conduction mode with high duty cycle values. This latter constraint imposes the use of a hysteretic comparator to perform the required modulation in the control loop without risk of saturation**.**

Hysteresis-based controllers are increasingly used to implement voltage regulation modules (VRMs) since they exhibit, at the expense of a variable switching frequency, a fast dynamic response in a wide regulation range with high duty cycle values. To design accurately this type of controllers in switching power converters, three techniques have been compared in [22]: a) describing function, b) Tsypkin's method, and c) sliding-mode control theory. It has been proved that the sliding- mode approach is the best solution and that it also allows a comprehensive description of the converter dynamics in the time domain. The sliding-mode control theory has been successfully applied in power switching converters, its applications ranging from voltage regulation in DC-DC power converters [23]-[30] and tracking of time varying current references [31]-[33], to control of the inrush current in the converter start-up [34].

The sliding-mode control is used in this approach to design a hysteresis-based quadratic boost converter that provides a regulated output voltage of 400 V DC from an input voltage in the range of 15 to 25 V DC. In this paper, the definition of a simple sliding surface for the regulation of the input inductor current yields the indirect control of the output voltage by forcing the mentioned current to reach a desired reference value in the equilibrium state. Therefore, if the current reference in the sliding surface is modified by the action of a PI compensator processing the output voltage error, it will be possible to regulate the output voltage to a desired level. Thus, the proposed controller consists of two loops, namely, an inner loop for input inductor current control

and an outer loop establishing the reference for the inner loop to ensure the output voltage regulation. Hence, to cope with the parameter uncertainty, a robust loop shaping method is chosen to synthesize the PI compensator with robustness constraints. The values of PI gains K_p and K_i are obtained for the stable range given by the Routh-Hurwitz stability test using a geometrical analysis in the Nyquist diagram involving the maximization of the integral gain [35]-[38]. This Robust Loop Shaping synthesis technique will be referred in the following as RLS-MIGO.

The rest of the paper is organized as follows. The quadratic boost converter model and the proposed control scheme are presented in section II. Next, the analysis of the sliding-mode current loop and the linearization of the ideal sliding dynamics are performed in section III. In section IV, the robust approach to synthesize the outer-loop compensator and the analysis of the parametric variations are presented. Simulation and experimental results verifying the effectiveness of the proposed control are reported in sections V and VI respectively. Finally, conclusions are given in section VII.

II. QUADRATIC BOOST CONVERTER AND PROPOSED CONTROLLER

The quadratic boost converter is a fourth-order structure with two commutation cells in synchronous operation. The first cell is composed of controlled switch S and diode *D1*, which constitute a boost converter stage together with inductor *L2* and capacitor *C2*. The second cell is composed of diodes *D3* and *D1*. As shown in Fig. 1, this converter has two circuit configurations for continuous conduction mode operation (CCM). In ON-state, switch *S* is on, diode *D2* is on and diodes *D1* and *D3* are off. In OFF-state, switch *S* is off, diode *D2* is off and diodes *D1* and *D3* are on. The bilinear model (1) is obtained from the differential equations derived for each converter state.

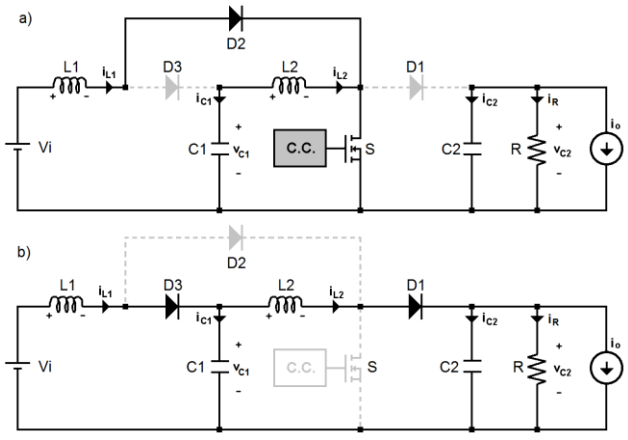

Fig. 1. Quadratic boost circuit configurations: a) ON-state; and b) OFF-state.

$$\begin{aligned}
\frac{di_{L1}}{dt} &= \frac{v_i}{L1} - \frac{v_{C1}}{L1}(1-u) \\
\frac{di_{L2}}{dt} &= \frac{v_{C1}}{L2} - \frac{v_{C2}}{L2}(1-u) \\
\frac{dv_{C1}}{dt} &= -\frac{i_{L2}}{C1} + \frac{i_{L1}}{C1}(1-u) \\
\frac{dv_{C2}}{dt} &= -\frac{v_{C2}}{RC2} + \frac{i_{L2}}{C2}(1-u) - \frac{i_0}{C2}
\end{aligned} \tag{1}$$

The control variable *u* is the gate signal of the controlled switch *S*, so that *u = 1* during ON-state and *u = 0* during OFF-state. Current source i_0 models the possible output load disturbances. Operation in CCM is guaranteed through the selection criteria for *L1, L2, C1* and *C2* values [39].

In steady-state i.e., derivatives equal to zero, the control variable u can be replaced in (1) by its average value represented by the duty cycle *D* yielding the relation.

$$\frac{v_{C1}}{v_i} = \frac{v_{C2}}{v_{C1}} = \frac{1}{1-D} \tag{2}$$

from which it can be deduced the ideal static transfer function of the converter *M(D).*

$$M(D) = \left(\frac{v_{C2}}{v_{C1}}\right)\left(\frac{v_{C1}}{v_i}\right) = \frac{1}{(1-D)^2} \tag{3}$$

Besides, input voltage perturbations, load variations and the uncertain value of the parasitic resistances in all components contribute to introduce voltage drops, deviating the actual output voltage of its expected value. Therefore, to obtain a regulated output voltage it is required a closed loop feed-back control system.

The presence of the right half-plane zeros in the dynamics of the high-order boost derived converters precludes the use of a single loop compensator processing the output voltage error. Therefore, the voltage regulation will be performed by a two-loop control scheme whose inner loop will process a fast variable like the input inductor current whereas the outer loop will establish the reference of the inner loop by treating a slow variable as the output voltage error [40]. Fig. 2 illustrates the hysteresis-based two-loop control, where the inner current loop is defined by means of a sliding surface S(x) and drives the converter to a stable equilibrium point.

The outer loop generates the required reference $I_E(t)$ at the output of a PI compensator in order to keep constant the coordinate of the output voltage in the equilibrium point in spite of input voltage perturbations or load changes. The dynamic behavior of $I_E(t)$ is considerably slower than that of the input inductor current and therefore it is possible to separate the analysis of inner and outer loops.

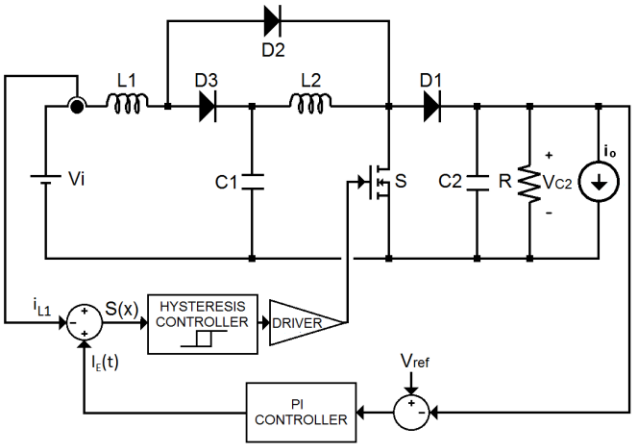

Fig. 2. General representation of the proposed control scheme.

III. Linear Modeling of the Ideal Sliding Dynamics

The control strategy in Fig. 2 is based on the sliding surface (4) which is defined using the input inductor current.

$$S(x) = i_{L1} - I_E(t) \tag{4}$$

where $I_E(t)$ is given by

$$I_E(t) = -K_p\left(v_{C2}(t) - V_{ref}\right) - K_i \int_{-\infty}^{t} \left(v_{C2}(\lambda) - V_{ref}\right) d\lambda \tag{5}$$

The switching function u yielding sliding motions is expressed as follows

$$u = \begin{cases} 1, & when\ S(x) < 0 \\ 0, & when\ S(x) > 0 \end{cases} \tag{6}$$

Evaluating the existence condition $S(x) \cdot \dot{S}(x) < 0$ using the control law (6) leads to the local reachability condition (7).

$$0 < v_i - L1\frac{dI_E}{dt} < v_{C1} \tag{7}$$

Applying the invariance conditions ($S(x) = 0$ *and* $\dot{S}(x) = 0$) [41] in (1) and (4) leads to the equivalent control

$$u_{eq} = 1 - \frac{1}{v_{C1}}\left(v_i - L1\frac{dI_E}{dt}\right) \tag{8}$$

By introducing both $S(x) = 0$ and the expression of the equivalent control in (1), the equation system (9) is obtained, which represents the resulting ideal sliding dynamics of the converter.

$$\begin{aligned}
\frac{di_{L2}}{dt} &= \frac{v_{C1}}{L2} - \frac{v_{C2}}{L2}\frac{1}{v_{C1}}\left(v_i - L1\frac{dI_E}{dt}\right) \\
\frac{dv_{C1}}{dt} &= -\frac{i_{L2}}{C1} + \frac{i_{L1}}{C1}\frac{1}{v_{C1}}\left(v_i - L1\frac{dI_E}{dt}\right) \\
\frac{dv_{C2}}{dt} &= -\frac{v_{C2}}{RC2} + \frac{i_{L2}}{C2}\frac{1}{v_{C1}}\left(v_i - L1\frac{dI_E}{dt}\right) - \frac{i_0}{C2}
\end{aligned} \tag{9}$$

By solving the equilibrium point of (9), considering that $i_E(t)$ has the constant value I_E, expression (10) is obtained.

$$\begin{aligned}
\overline{i_{L1}} &= I_E; & \overline{i_{L2}} &= I_E^{\frac{3}{4}}(v_i/R)^{\frac{1}{4}}; \\
\overline{v_{C1}} &= (I_E R)^{\frac{1}{4}} v_i^{\frac{3}{4}}; & \overline{v_{C2}} &= (I_E v_i R)^{\frac{1}{2}}
\end{aligned} \tag{10}$$

It is possible to show that under the conditions $v_{C1} > \frac{1}{4}\overline{v_{C1}}$ and $i_{L2} < 2\overline{i_{L2}}$, the inner loop (i.e. $I_E(t) = constant = I_E$) with the associated equilibrium point given by (10) is asymptotically stable (see Appendix). It is worth noting that the region delimited by $v_{C1} > \frac{1}{4}\overline{v_{C1}}$ and $i_{L2} < 2\overline{i_{L2}}$ covers an important domain of the system operation. However, proving the stability of the overall

system (i.e., the converter controlled by the two loops) is a difficult task, so that in the sequel only an analysis based on linearization (first method of Lyapunov) is provided, this approach being classically adopted in several studies [30].

By linearizing (9) around the equilibrium point (10), the equation system (11) is obtained where the superscript (~) stands for the increments of the variables in (9) around the corresponding equilibrium values.

$$\begin{aligned}
\frac{d\widetilde{i_{L2}}}{dt} &= \frac{2}{L2}\widetilde{v_{C1}} - \frac{\overline{v_\iota}}{L2\overline{v_{C1}}}\widetilde{v_{C2}} + \frac{L1\overline{v_{C2}}}{L2\overline{v_{C1}}}\frac{d\widetilde{i_E}}{dt} - \frac{\overline{v_{C2}}}{L2\overline{v_{C1}}}\widetilde{v_\iota} \\
\frac{d\widetilde{v_{C1}}}{dt} &= \frac{-1}{C1}\widetilde{i_{L2}} - \frac{\overline{i_E}}{C1\overline{v_{C2}}}\widetilde{v_{C1}} + \frac{\overline{v_\iota}}{C1\overline{v_{C1}}}\widetilde{i_E} - \frac{L1\overline{i_E}}{C1\overline{v_{C1}}}\frac{d\widetilde{i_E}}{dt} + \frac{\overline{i_E}}{C1\overline{v_{C1}}}\widetilde{v_\iota} \\
\frac{d\widetilde{v_{C2}}}{dt} &= \frac{\overline{v_\iota}}{C2\overline{v_{C1}}}\widetilde{i_{L2}} - \frac{\overline{i_{L2}}}{C2\overline{v_{C2}}}\widetilde{v_{C1}} - \frac{1}{RC2}\widetilde{v_{C2}} - \frac{L1\overline{i_{L2}}}{C2\overline{v_{C1}}}\frac{d\widetilde{i_E}}{dt} + \frac{\overline{i_{L2}}}{C2\overline{v_{C1}}}\widetilde{v_\iota} - \frac{1}{C2}\widetilde{i_0}
\end{aligned} \tag{11}$$

By applying the Laplace transform to (11), the polynomial function (12) is obtained

$$A(s)V_{C2}(s) = B(s)I_E(s) + C(s)V_i(s) - D(s)I_0(s) \tag{12}$$

where $V_{C2}(s)$ is the linearized system output, $I_E(s)$ is the corresponding input , and $I_0(s)$ and $V_i(s)$ represent an output load disturbance and an input voltage perturbation respectively. The terms $A(s)$, $B(s)$, $C(s)$ and $D(s)$ are defined as (13), (14), (15) and (16) respectively.

$$A(s) = L2C2\overline{v_{C2}}s^3 + T_{L2}\overline{v_{C2}}\left(K_m\frac{C2}{C1} + 1\right)s^2 + \left[\overline{v_{C2}}\left(2\frac{C2}{C1} + K_m\frac{T_{L2}}{T_{C1}}\right) + \overline{v_\iota}\right]s + \frac{4\overline{v_{C2}}}{T_{C1}} \tag{13}$$

$$B(s) = K_m T_{L1}T_{L2}R\overline{v_{C2}}s^3 + T_{L1}R\overline{v_{C2}}s^2 + \frac{K_m R}{T_{C1}}(2T_{L1}\overline{v_{C2}} + T_{L2}\overline{v_\iota})s + \frac{2R\overline{v_\iota}}{T_{C1}} \tag{14}$$

$$C(s) = K_m T_{L2}\overline{v_{C2}}s^2 - \overline{v_{C2}}s + \frac{2K_m\overline{v_{C2}}}{T_{C1}} \tag{15}$$

$$D(s) = T_{L2}R\overline{v_{C2}}s^2 - \frac{K_m T_{L2}R\overline{v_{C2}}}{T_{C1}}s + \frac{2R\overline{v_{C2}}}{T_{C1}} \tag{16}$$

where $K_m = \overline{v_{C2}}/\overline{v_{C1}} = \overline{v_{C1}}/\overline{v_i}$, $T_{L1} = L1/R$, $T_{L2} = L2/R$, $T_{C1} = R\,C1$, $T_{C2} = R\,C2$ and superscript $(-)$ represents the equilibrium values of the state variables. Thus, by nullifying the dynamics of both disturbances, it is possible to obtain the transfer function from the incremental input inductor current to the incremental output voltage

$$G_{ie}(s) = \frac{V_{C2}(s)}{I_E(s)} = \frac{B(s)}{A(s)} \tag{17}$$

Likewise, by nullifying the dynamics of the input current and one of the disturbances, it is possible to obtain the transfer function from either the input voltage variation or the output load perturbation to the incremental output voltage, given by (18) and (19) respectively.

$$G_{vi}(s) = \frac{V_{C2}(s)}{V_i(s)} = \frac{C(s)}{A(s)} \tag{18}$$

$$G_{io}(s) = \frac{V_{C2}(s)}{I_o(s)} = -\frac{D(s)}{A(s)} \tag{19}$$

IV. Synthesis of the Voltage Regulation Loop

Although the sliding-mode control inherently gives robustness to the controlled system, the existence of the outer compensator drastically changes the overall dynamics of the converter variables, and therefore the robustness has to be guaranteed by an appropriate selection of the compensator parameters. Hence, to synthesize the controller parameters, the Routh-Hurwitz test is used first to establish the main design constraints [42].

A. Determination of a local stability region

The PI compensator in the outer loop is defined by the transfer function

$$G_c(s) = K_p + \frac{K_i}{s} \tag{20}$$

Therefore, the loop-gain transfer function is $L(s) = G_c(s)G_{ie}(s)$ while the closed- loop transfer function from reference voltage to output voltage is given by

$$G_{vo}(s) = \frac{G_c(s)B(s)}{A(s) + G_c(s)B(s)} \tag{21}$$

Therefore, the characteristic polynomial is given by

$$P(s) = s\big(A(s) + G_c(s)B(s)\big) \tag{22}$$

By defining $A(s) = a_3s^3 + a_2s^2 + a_1s + a_0$, and $B(s) = b_3s^3 + b_2s^2 + b_1s + b_0$, it is obtained that

$$P(s) = p_4s^4 + p_3s^3 + p_2s^2 + p_1s + p_0 \tag{23}$$

where $p_0 = b_0K_i$, $p_1 = a_0 + b_1K_i + b_0K_p$, $p_2 = a_1 + b_2K_i + b_1K_p$, $p_3 = a_2 + b_3K_i + b_2K_p$, $p_4 = a_3 + b_3K_p$. Thus, by applying the Routh-Hurwitz stability test, the resulting array is given in Table I.

TABLE I

ROUTH-HURWITZ STABILITY RESULTING ARRAY

s^4	p_4	p_2	p_0
s^3	p_3	p_1	0
s^2	$(p_2p_3 - p_1p_4)/p_3$	p_0	0
s^1	$(p_1p_2p_3 - {p_1}^2p_4 - p_0{p_3}^2)/p_3$	0	0
s^0	p_0	0	0

Therefore, in order to have a stable system, it is necessary to guarantee the fulfillment of conditions in (24).

$$\begin{aligned} &p_0 > 0;\ p_1 > 0;\ p_2 > 0;\ p_3 > 0;\ p_4 > 0; \\ &p_2p_3 - p_1p_4 > 0;\ p_1p_2p_3 - {p_1}^2p_4 - p_0{p_3}^2 > 0 \end{aligned} \tag{24}$$

From the above procedure, a stable region in the K_p - K_i plane is delimited by conditions $p_0 > 0$, $\mathrm{p}_2 > 0$, $p_2p_3 - p_1p_4 > 0$ and $p_1p_2p_3 - {p_1}^2p_4 - p_0{p_3}^2 > 0$. Solving $\mathrm{p}_0 >$

0 directly renders $K_i > 0$ and solving $p_2 > 0$ implies $K_p > 0$. Further, solving $p_2 p_3 - p_1 p_4 > 0$, a second-degree equation corresponding to a hyperbole in the K_p - K_i plane is identified. Finally, solving $p_1 p_2 p_3 - {p_1}^2 p_4 - p_0 {p_3}^2 > 0$ a third-degree relation is also identified. Fig. 3 shows the evaluation of the stability conditions for a constant operational point and the resulting stability region.

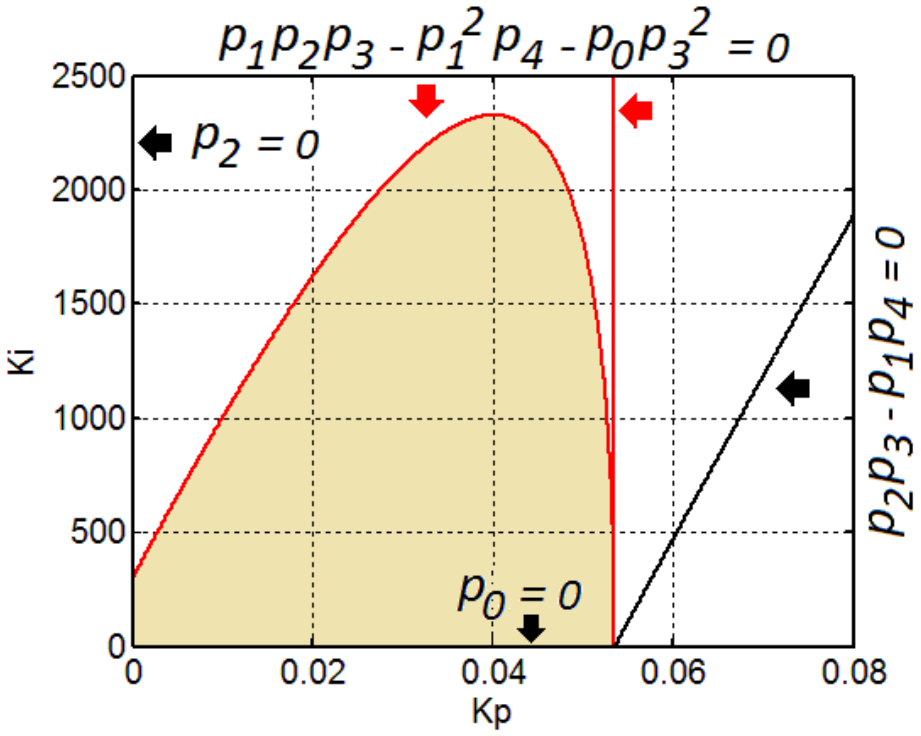

Fig. 3. Evaluation of the stability region in the K_p - K_i plane using $L1 = 120\ \mu H$, $L2 = 4.7 mH$, $C1 = C2 = 9\ \mu F$, $R = 8\ k\Omega$ $v_i = 25\ V$, $\overline{v_{C2}} = 400\ V$.

Hence, the synthesis of the PI compensator must provide a solution within this region for all operational conditions in order to ensure stability.

B. Robust loop shaping design method with integral gain maximization (RLS-MIGO)

The controller design is based on the Nyquist diagram which can be used to relate a robustness region with both the sensitivity function $S(j\omega)$ and the complementary sensitivity function $T(j\omega)$. Hence, by defining $M_s = \sup_{\omega} |S(j\omega)|$ and $M_t = \sup_{\omega} |T(j\omega)|$, the closed loop system will be asymptotically stable if the Nyquist curve of the loop function $L(s)$ is outside a circle whose center *c* and radius *r* are defined as illustrated in the two first rows in Table II.

TABLE II

CENTERS AND RADIUS OF THE CIRCULAR ROBUSTNESS REGIONS FOR CONSTANT SENSITIVITIES [36]

Contour	Center	Radius
M_s	-1	$\frac{1}{M_s}$
M_t	$-\frac{{M_t}^2}{{M_t}^2-1}$	$\frac{{M_t}^2}{{M_t}^2-1}$
M_s, M_t	$\frac{M_s(2M_t-1)-M_t}{2M_s(1-M_t)}$	$\frac{M_s+M_t-1}{2M_s(1-M_t)}$
$M=M_s=M_t$	$-\frac{2M^2-2M+1}{2M(M-1)}$	$\frac{2M-1}{2M(M-1)}$

By combining these constraints, the Nyquist curve of the function $L(s)$ must be outside of the circle defined by the characteristics in the fourth row of Table II. Using this criterion, the values of M_s and M_t are equal to the value M. Numerically, if the Nyquist curve of the loop function never crosses the boundary defined by a value of M between 1.4 and 2, it is possible to assure immunity against disturbances, nonlinearities and large parameter variations [38]. It is worth to mention that the combined sensitivity criteria are derived from the relation between the robust loop shaping method and the frequency weighting of the H_∞ norm when equal values of M_s and M_t are considered [35].

From the last definition, the design problem of the outer PI loop consists in computing K_p and K_i with the constraint for the combined sensitivity M. Then, the robustness condition is given by the following expression [36]

$$\left(K_p+\frac{cos\big(\varphi(\omega)\big)}{\rho(\omega)}c\right)^2+\frac{1}{\omega^2}\left(K_i+\frac{sin\big(\varphi(\omega)\big)}{\rho(\omega)}c\omega\right)^2\geq\frac{r^2}{\rho(\omega)^2} \tag{25}$$

where $\rho(\omega)$ and $\varphi(\omega)$ are functions of the ω representing the magnitude and phase of the converter transfer function according to expression (26).

$$G(j\omega) = \frac{B(j\omega)}{A(j\omega)} = \rho(\omega)e^{j\varphi(\omega)} = \rho(\omega)\left[cos\left(\varphi(\omega)\right) + jsin\left(\varphi(\omega)\right)\right] \quad (26)$$

It is worth to note that the locus of the solution of equation (25) for fixed ω is an ellipse, whose parameters are also functions of ω. Then, in a high-order system, such as the quadratic boost converter, a space of infinite solutions is obtained, so that the choice of the controller parameters results in an optimization problem. To solve it, an algorithm has been developed to find solutions in the stability region initially determined by the Routh-Hurwitz test. The best solution is then selected through the maximization of the integral component in the sense of the M-constrained integral gain optimization method (RLS-MIGO) described in [38], since this criterion can be interpreted as the minimization of the integral error against load disturbances. Then, the corresponding optimization problem is expressed as

$$\left| \begin{array}{c} Max\ K_i \\ K_p, K_i \in Stability\ Region\ (Routh - Hurwitz\ test) \\ such\ that\ (24)\ and\ (25) \end{array} \right. \quad (27)$$

To solve it, define ω_{int} as the frequency for which the Nyquist curve borders the boundary of the robustness region. The idea is to vary ω_{int} in a defined range $R\omega_{int}$ and for each value ω_{int}, to the RLS-MIGO method. Among all the obtained couples (K_p, K_i), the solution which maximizes the integral gain K_i is retained. To summarize the following steps are implemented:

1) Select a value for M (generally $1.4 \leq M \leq 2$) and compute the corresponding center c and radius r of the circular robustness region.
2) Define a discrete frequency range $R\omega_{int}$.
3) Use the Routh-Hurwitz stability test delimiting the stability region, and define a discrete range for K_p, say RK_p (See figure 5).
4) For each value $\omega_{int} \in R\omega_{int}$:
   - Compute $\rho(\omega_{int})$ and $\varphi(\omega_{int})$.
   - Compute K_i sweeping K_p into RK_p using (25) (An ellipse is generated).
5) Determine the admissible K_p, K_i region which corresponds to the intersection between the domains outside all ellipses and the stability region (robust-stability region in figure 5).

6) Among all the possible solutions, retain the stable solution which maximizes K_i ($K_{i_{max}}$ in figure 5).

After applying the proposed method, stability and robustness have been delimited in the same K_p and K_i plane giving a comprehensive approach for this complex control synthesis problem. Note that after linearization the resulting transfer function has right half-plane zeros, this increasing the complexity of the synthesis process. However, on the basis of the robustness concept in the loop shaping method and the local stability of the Routh-Hurwitz test, it is possible to ensure the stability of the controlled system.

C. Selection of the controller parameters

By closing the loop in the converter dynamics represented by (12) with the inclusion of the PI compensator, the resulting closed-loop controlled system can be modeled by the block diagram shown in Fig. 4.

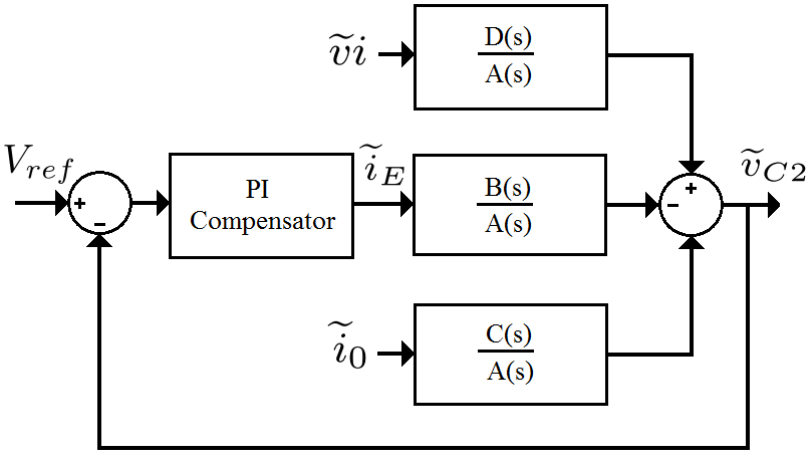

Fig. 4. Equivalent block diagram for the output voltage regulation loop considering a linearized model of the ideal sliding dynamics.

The PI synthesis method is applied in a 100 W quadratic boost converter delivering a regulated output voltage of 400 V for a nominal input voltage of 20 V. The passive parameters of the converter are $L1 = 120\ \mu H, L2 = 4.7\ mH, C1 = C2 = 9\mu F$.

The RLS-MIGO method is applied taking values of ω_{int} between 39 and 304 Rad/s. For a constant mixed sensitivity of 2, a radius $r = 0.75$ and a center c in the coordinate (-1.25, 0) have been obtained. The converter transfer function has been evaluated for the nominal values of the output power and input voltage.

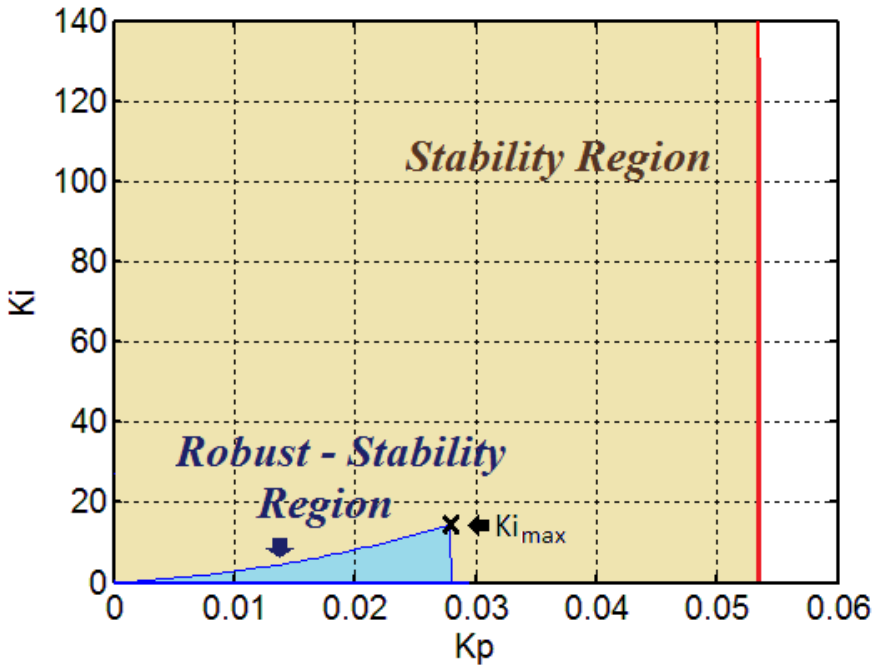

Fig. 5. Stability and robustness regions superimposed showing the solution which maximizes K_i ($K_p = 0.0268$, $K_i = 13.3$).

As shown in figure 5, RLS-MIGO method gives an admissible region in the K_p - K_i plane which ensures stability and robustness. All solutions maximizing K_i for different intersection frequencies are related by the envelope generated by superposing the ellipse solutions. Table III shows some of K_p and K_i controller parameters related with its corresponding intersection frequencies ω_{int}.

TABLE III

PI CONTROLLER PARAMETERS FOR DIFFERENT CHOICES OF ω_{int}

ω_{int}	K_p	K_i
39 Rad/seg	0.0001	0.23
50 Rad/seg	0.001	0.37
90 Rad/seg	0.005	1.22
140 Rad/seg	0.01	2.91
179 Rad/seg	0.014	4.7
235 Rad/seg	0.020	8.2
283 Rad/seg	0.025	11.9
304 Rad/seg	0.0268	13.3

Fig. 6 depicts the Nyquist diagram showing the curves of the $L(s)$ function for the three values of ω_{int}. It can be observed that all curves accomplish the design constraint.

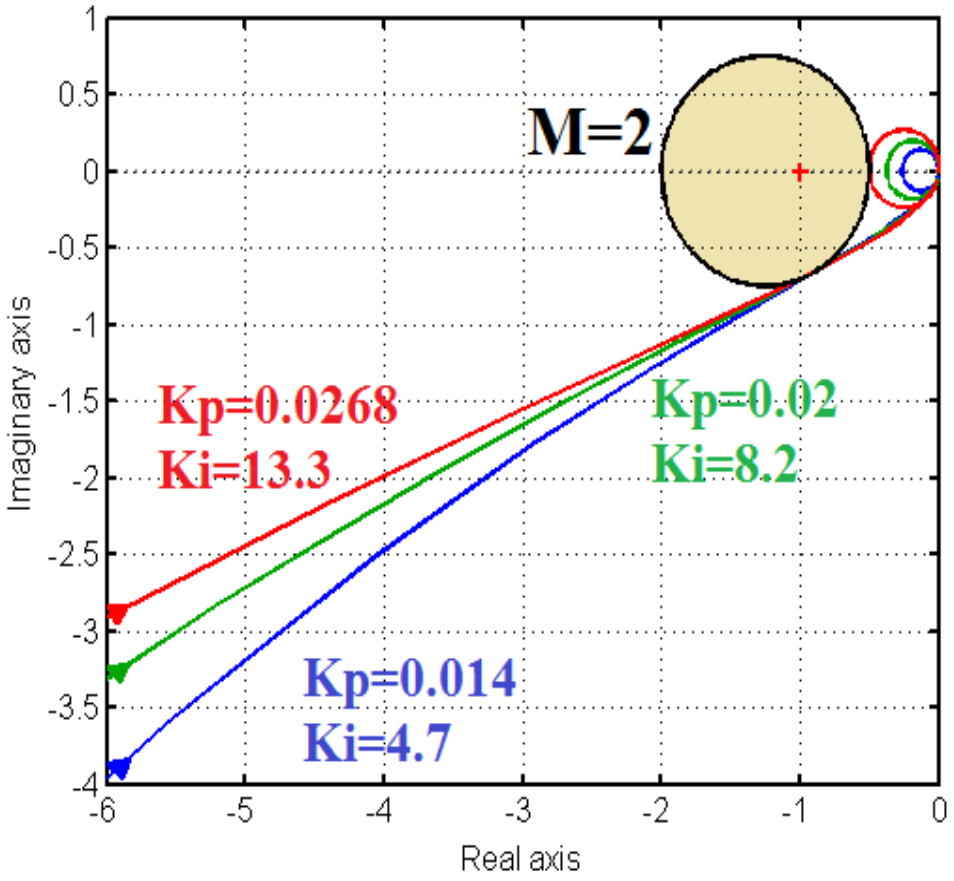

Fig. 6. Nyquist curves showing the solution of the PI design problem for ω_{int} = 179, 235 and 304 Rad/s.

D. Parameter variation analysis

By replacing the polynomials $A(s)$ and $B(s)$, given by (13) and (14) respectively, in the input current to output voltage transfer function (17), expression (27) is derived

$$G_{ie}(s) = \frac{-\frac{{K_m}^2 L1}{RC2}s^3 + \frac{L1}{L2C2}s^2 - \left(\frac{2{K_m}^2 L1 + L2}{R\,L2\,C1\,C2}\right)s + \frac{2}{{K_m}^2 L2C1C2}}{s^3 + \left(\frac{{K_m}^2 C2 + C1}{R\,C1\,C2}\right)s^2 + \left(\frac{2{K_m}^2 R^2 C2 + {K_m}^4 L2 + R^2 C1}{{K_m}^2 R^2 L2\,C1\,C2}\right)s + \frac{4}{RL2C1C2}} \quad (27)$$

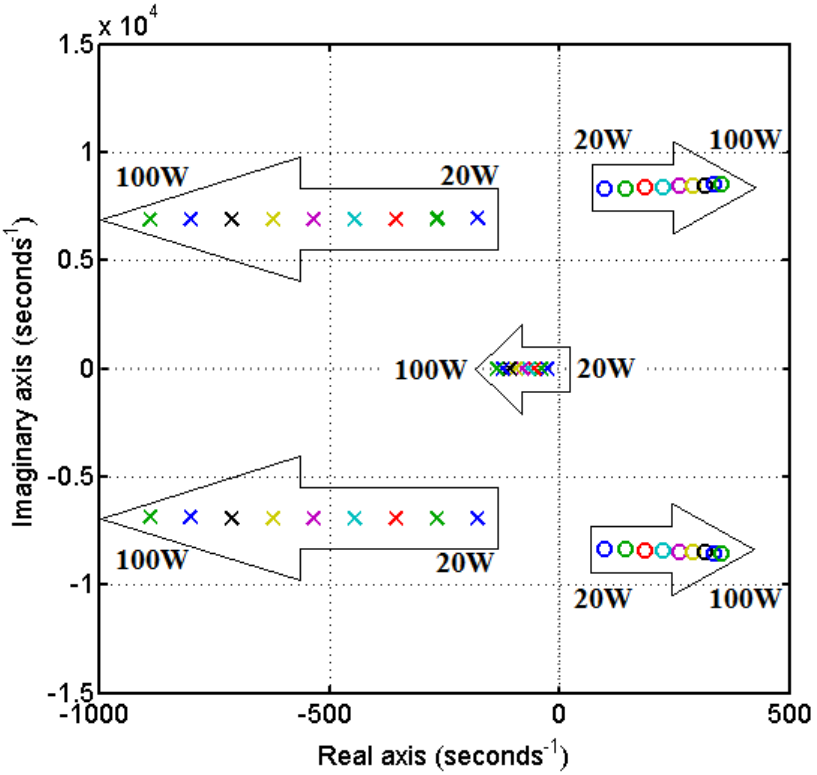

Fig. 7. Equilibrium point loci for a constant input voltage and a variable output power.

Since the transfer function $G_{ie}(s)$ has been obtained from the linearization of the ideal sliding dynamics, the numerator and denominator coefficients will have a clear dependence on the equilibrium point coordinates as it can be observed in (27) by the presence of K_m and R in the polynomial coefficients. Fig. 7 shows the root locus of $G_{ie}(s)$ for a constant input voltage of 15 V, a regulated value of 400 V in the output voltage and values of output power changing from 20 to 100 W with steps of 10 W. It can be observed that the system poles hardly change whereas the zeros undergo significant displacements. On the other hand, Fig. 8 shows the root locus of $G_{ie}(s)$ for a constant output power of 100 W using input voltage values changing from 15 to 25 V with steps of 2.5 V. It is worth pointing out that only two zeros are shown in figures 6 and 7 since the third zero has always non-minimum phase and is too far from the origin.

An analysis in the overall operational range of the converter has been developed to illustrate the performance of the RLS-MIGO solution versus the parameter variation. The solution for $\omega_{int} = 304\ Rad/s$ has been selected, which corresponds to a K_p of 0.0268 and a K_i of 13.3, since this solution maximizes the integral gain in the selected frequency range.

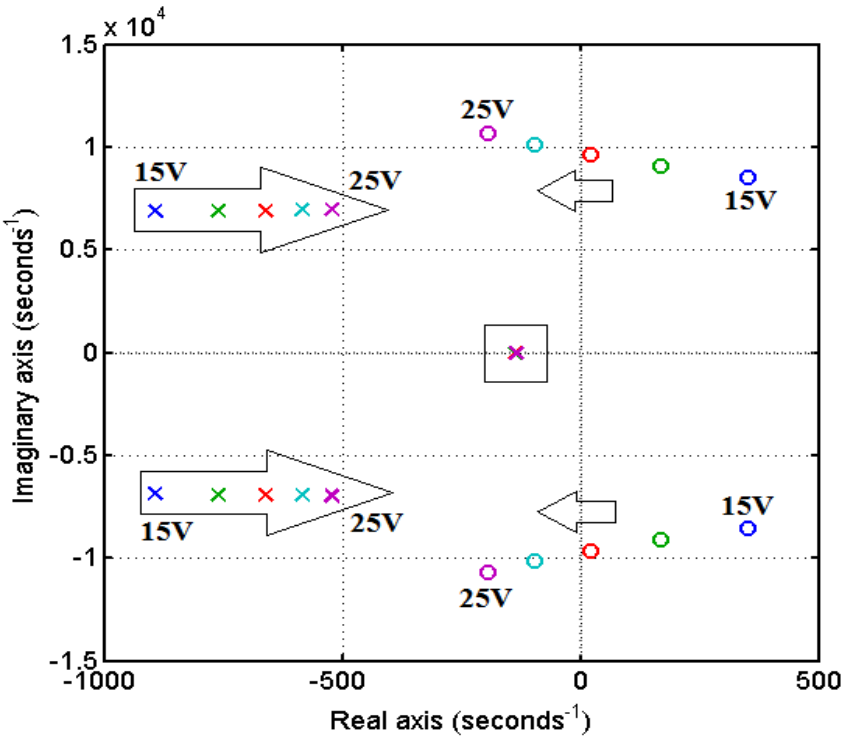

Fig. 8. Equilibrium point loci for a constant output power and variable input voltage.

Fig. 9 shows the Nyquist curves resulting of a test covering the overall operational range of both input voltage and output power. The voltage range is covered by using 1 V steps and the output power by employing 10 W steps. It can be observed that the Nyquist curves remain distant of the critical point -1 for any condition. Also, the Nyquist curves for the worst cases penetrate into the robustness region just until the limit of the contour defined by a combined sensitivity of 1.4, which is also considered a picky parameter to deal with other uncertainties. Hence, it is possible to conclude that the converter is stable showing robustness to parametric variation.

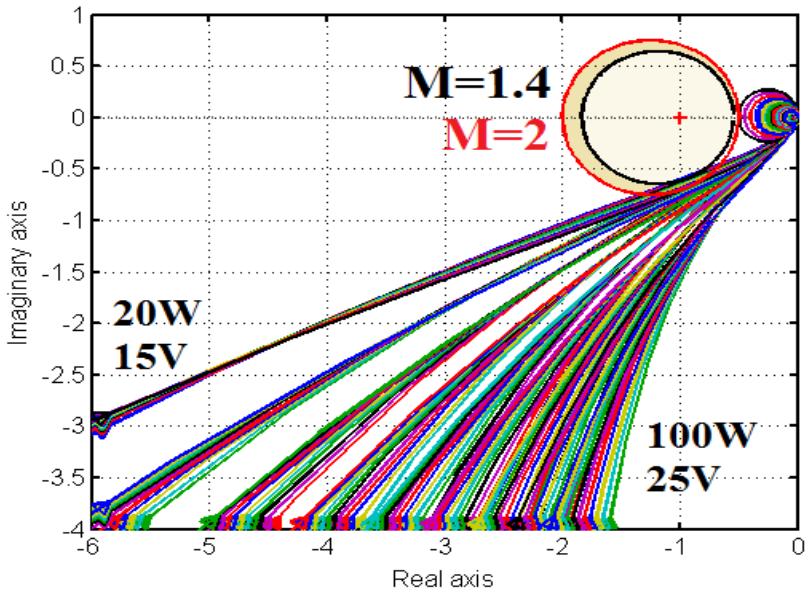

Fig. 9. Robustness regions for $M = 2$ (Outer circle in red color) and $M = 1.4$ (inner circle in black color) related with Nyquist curves for loop-gain transfer functions obtained with the PI controller $K_p = 0.0268$ and $K_i = 13.3$ in the overall range of parameter variation.

As shown in table IV, the equilibrium values of the currents in the regulated converter depend on both load and input voltage while the equilibrium value of capacitor voltage in *C1* only depends on the input voltage because of the constant value in the output voltage forced by the regulation loop. Further, it is possible to observe the wide range of DC-gain which has been explored in this application, which constitutes one of the important achievements in this work.

TABLE IV

DIFFERENT EQUILIBRIUM POINTS AND DERIVED PARAMETERS

COVERING THE OVERALL OPERATIONAL RANGE

$V_{C2}\ (V)$	$V_i\ (V)$	K_m	${K_m}^2$	$V_{C1}(V)$	$P\ (W)$	$I_{L1}(A)$	$I_{L2}\ (A)$	$R\ (\Omega)$
400	15	5,16	26,6	77,46	20	1,33	0,26	8 k
					50	3,33	0,64	3,2 k
					100	6,67	1,29	1,6 k
	20	4,47	19.98	89,44	20	1,00	0,22	8 k
					50	2,50	0,56	3,2 k
					100	5,00	1,12	1,6 k
	25	4	16	100	20	0,80	0,2	8 k
					50	2,00	0,5	3,2 k
					100	4,00	1,0	1,6 k

V. SIMULATION RESULTS

In this section, results of MATLAB- based simulation verifying analytical predictions are given. Output load and input voltage disturbances are applied considering the operation of the converter in an extreme equilibrium point of its working range.

A. Output power disturbance rejection

A perturbation in the output current is applied to evaluate the load disturbance rejection capability of the control loop. Fig. 10 shows a zoom of the simulation results for a step disturbance of 62.5 mA (25% of the nominal load) which is applied when the converter operates in different equilibrium points. Note that the disturbance produces a transient deviation of the output voltage below 5% which is totally rejected in less than 72 ms for the worst case.

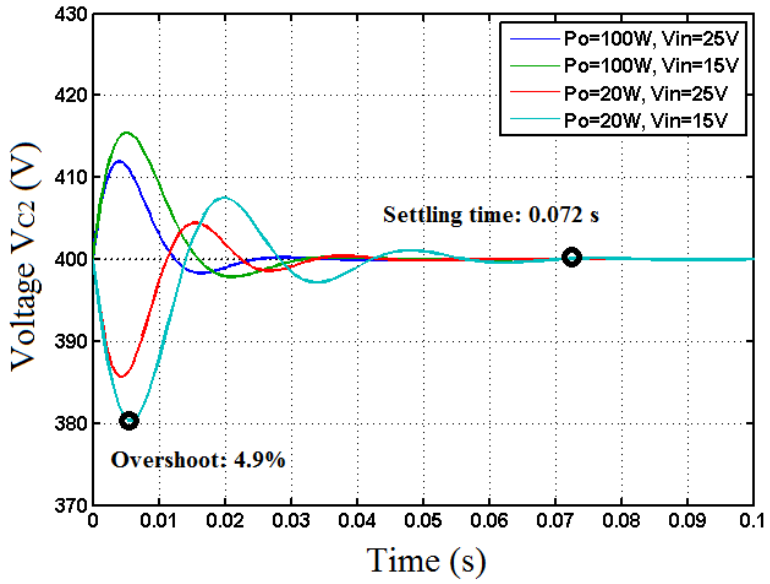

Fig. 10. Transient responses to output power step disturbances in the extreme values of the converter operational range.

B. Input voltage disturbance rejection

An input voltage disturbance of step type of 5 V is also applied to the converter. For an initial value of 15 V in the input voltage the disturbance is considered positive, whereas in the cases with an initial value of 25 V in the input voltage, the disturbance is considered negative. It can be seen in Fig. 11 that the disturbances are rejected in approximately 62 ms showing a maximum transient voltage deviation below 6% for all cases.

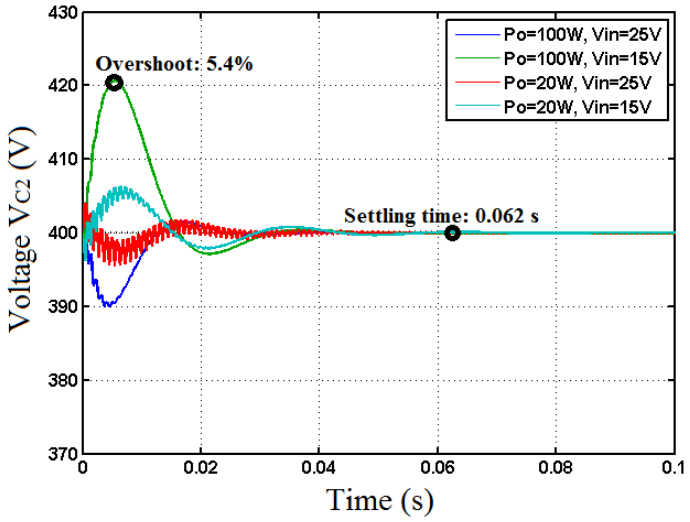

Fig. 11. Transient response to input voltage step disturbances in the extreme values of the converter operational range.

C. Set-point change transient response

Fig. 12 shows the step response to a 60 V change applied in the voltage reference when the converter is in steady-state with a regulated output voltage of 400 V. This change produces a maximum deviation in the output voltage below 45% relative to the reference excitation, and a settling time of approximately 72 ms for all cases. It is worth noting that once the effect of the set-point change disappears the converter regulates again the output voltage at the new reference value without error.

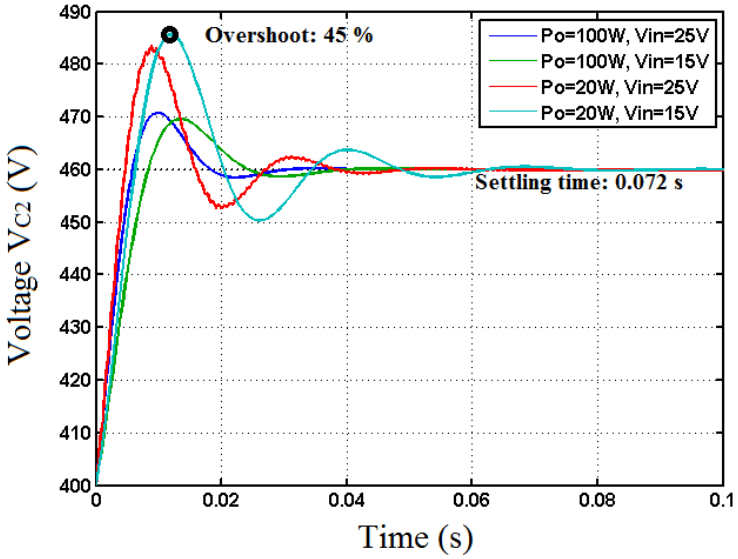

Fig. 12. Transient response to a voltage reference step change in the extreme values of the converter operational range.

These simulation results show that despite its high DC-gain, the converter is capable to reject important disturbances in the input voltage and output load without significant deviations or poor transient behavior. Note also that when the converter copes with important disturbances, the ratio between the magnitude of the overshoot and the steady-state values of the output voltage is significantly small. It is worth mentioning that a change in the value of the output voltage reference leads to important over-shoots as shown in Fig. 12. Nonetheless, it has to be pointed out that in a normal operation the value of the output voltage reference does not change.

VI. EXPERIMENTAL RESULTS

In order to obtain the experimental validation of the design, a quadratic boost converter prototype has been implemented. The converter is designed to regulate 400 V for an input voltage range from 15 to 25 V and an output load range from 20 to 100 W. The set of converter parameters is the same used in sections IV and V ($L1 = 120\,\mu H$, $L2 = 4.7\,mH$ and $C1 = C2 = 9\mu H$). Capacitors *C1* and *C2* are of film type C4ATHBW4900A3LJ from KEMET with an ultra-low series resistance (1.9 mΩ) and capability to handle high voltages in switching applications. The MOSFET APT94N60L2C3 with CoolMOS technology has been selected to implement the switch *S* since it offers an ultra-low ON-resistance (0.035 Ω) and an ultra-low gate charge (550 nC). Besides, SiC Schottky diodes have been used to reduce the switching losses due to the absence of recovery charge. The silicon carbide Schottky diode C3D06060A from CREE has been selected to implement *D1* whereas the Schottky diode IDT16S60C from Infineon has been chosen to implement diodes *D2* and *D3*. A maximal efficiency of 92% has been obtained with this set of components.

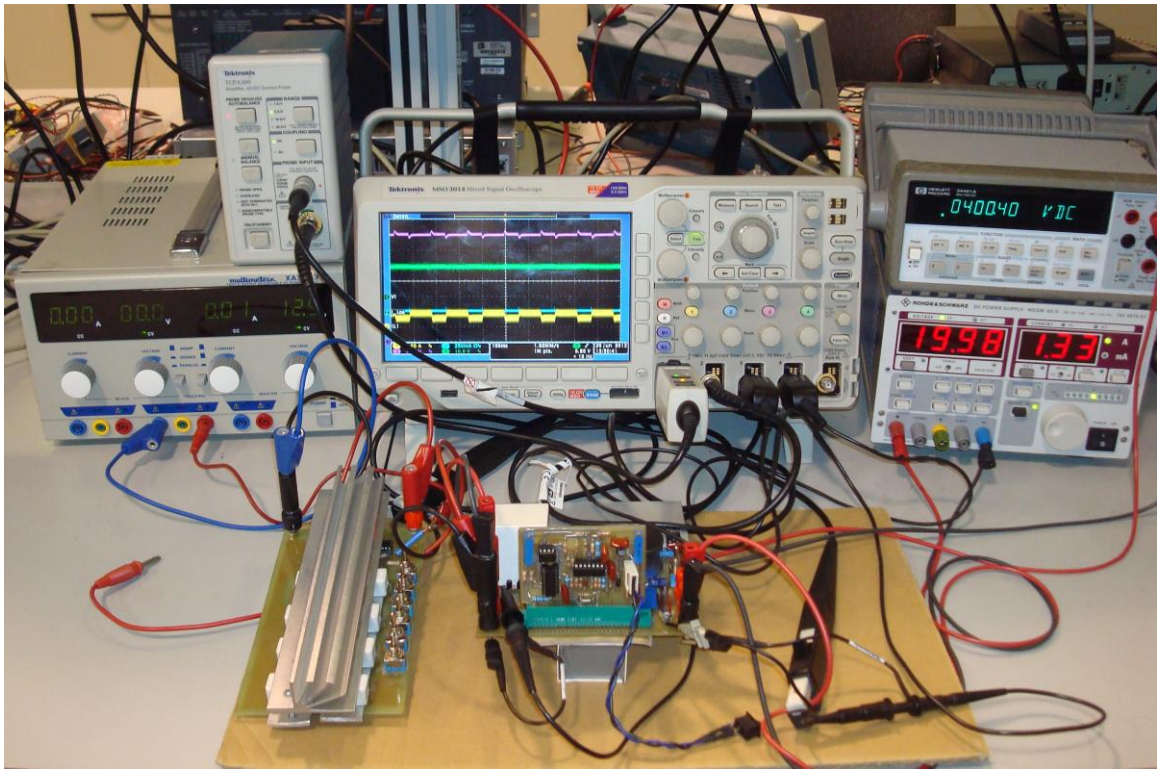

Fig. 13. Experimental set-up and prototype of the quadratic boost converter

The set-up for measurements shown in Fig. 13 is composed of the oscilloscope MSO3014 from Tektronix, the current probes TCP202 and TCPA300 from Tektronix, power supplies Rohde & Schwartz NGSM 60/5 and Multimeteix XA3033, and multimeter HP34401A from Hewlett Packard. Also, the frequency response meter 3120 from Venable Instruments has been used to obtain experimentally the Nyquist curves. The schematic circuit diagram of the resulting controller is shown in Fig. 14.

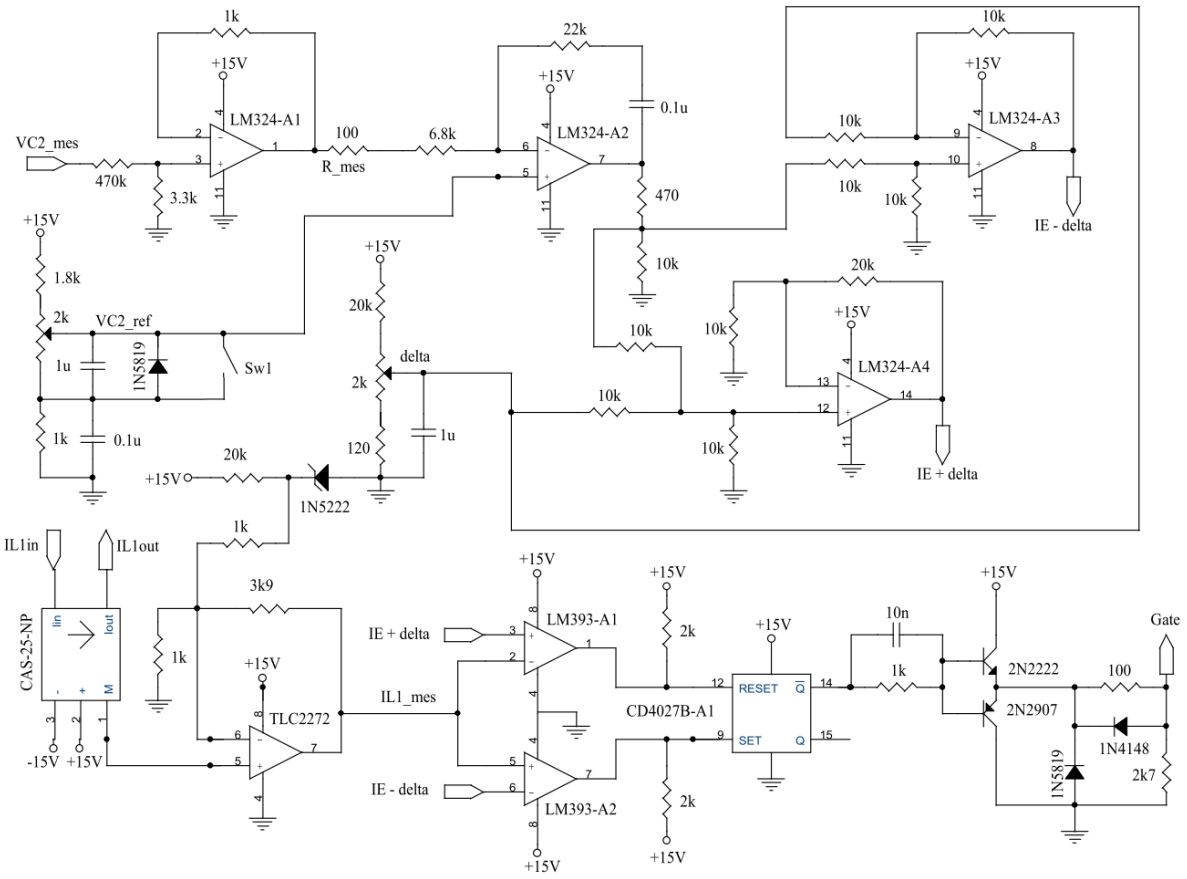

Fig. 14. Detailed circuit implementation of the robust sliding-mode based two-loop controller.

Note that the sliding-mode control theory requires an ideal comparator for its implementation, which implies an infinite switching frequency. However, from a practical point of view a hysteretic comparator is needed because the power devices cannot switch at infinite frequency and the use of an ideal comparator would lead to wrong decisions if some noise were added to any of its inputs. Therefore, the sliding-mode controller has been implemented by means of a hysteresis comparator based on a flip-flop circuit and two comparators. Thus, the control law (6) is finally implemented as

$$u = \begin{cases} 1, & when\ S(x) < -\delta \\ 0, & when\ S(x) > \delta \end{cases} \tag{28}$$

Then, the hysteresis band has the limits $i_E(t) + \delta$ and $i_E(t) - \delta$ where a value of 0.75 A has been selected for δ to constrain the switching frequency from 66 kHz to 130 kHz, which is compatible with the best efficiency levels of the converter [12].

The output voltage sensor employs a simple voltage divider while the input current sensor uses the Hall-effect sensor CAS25-NP from LEM. A transistor- based circuit has been implemented to drive the gate signal of the MOSFET. The switch Sw1 is used to apply a step change of the reference for the output voltage whereas the resistance R_mes allows frequency response measurement tests. Signal VC2_ref is the output of a soft-start circuit which provides a steady-state reference value in less than 200 ms after start-up.

A. Output power disturbance rejection

Step disturbances of 62.5 mA (25% of the nominal load) have been applied to the converter prototype. For an initial value of 20 W in the output power the disturbance is considered positive, whereas in the cases with an initial value of 100 W in the output power, the disturbance is considered negative. Note in Fig. 15 that the disturbance produces a maximum transient deviation of the output voltage always below 5%, which is rejected in less than 40 ms in the worst case. Note also that the output voltage returns to 400 V after a fast transient-state.

B. Input voltage disturbance rejection

Input voltage disturbances of step type of 5 V (25% of the nominal value) have been applied to the converter prototype operating in extreme equilibrium points. For an initial value of 15 V in the input voltage the disturbance is considered positive, whereas in the cases with an initial value of 25 V in the input voltage, the disturbance is considered negative. It can be seen in Fig. 16 that the disturbances are rejected in less than 40 ms with a maximum transient voltage deviation below 3.5% in all cases. Note also that, after the transient state, the output voltage returns to 400 V showing a perfect tracking of the voltage reference.

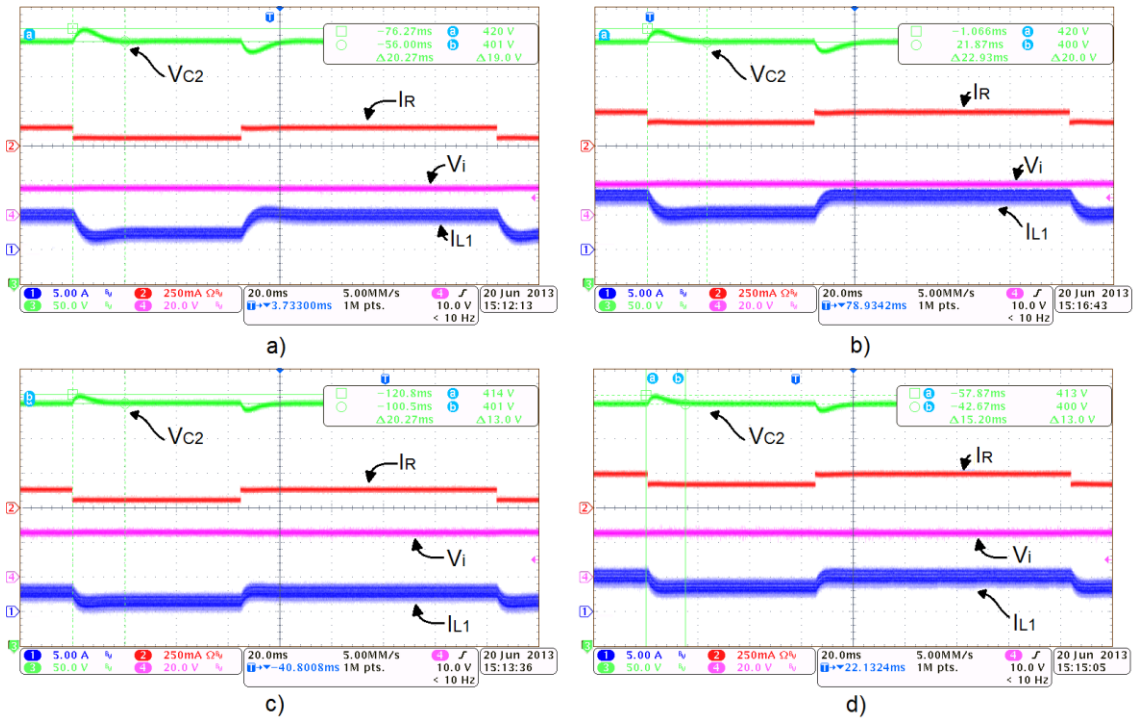

Fig. 15. Experimental waveforms for step disturbances on the output power with constant input voltage: a) 25 W – 50 W – 25 W disturbances operating with an input voltage of 18 V; b) 100 W – 75 W – 100 W disturbances operating with an input voltage of 18 V; c) 25 W – 50 W – 25 W disturbances operating with an input voltage of 25 V; d) 100 W – 75 W – 100 W disturbances operating with an input voltage of 25 V.

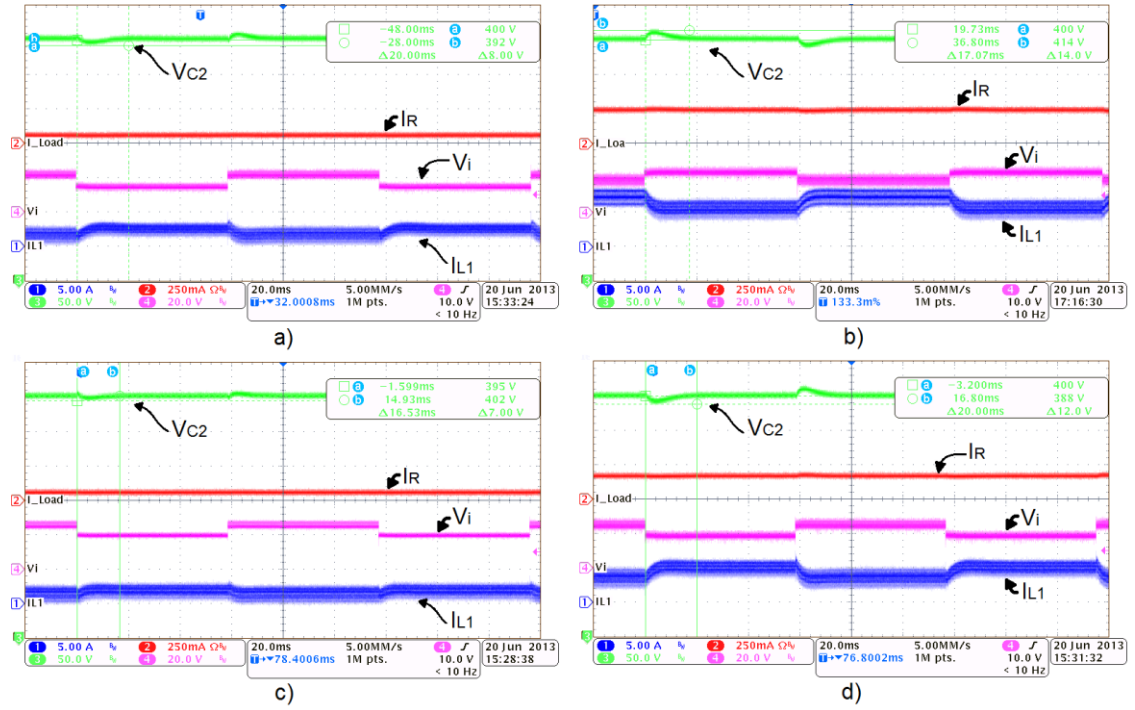

Fig. 16. Experimental waveforms for step disturbances on the input voltage with constant output load: a) 15 V – 20 V – 15 V disturbances operating with an output load of 25 W; b) 15 V – 20 V – 15 V disturbances operating with an output load of 100 W; c) 25 V – 20 V – 25 V disturbances operating with an output load of 25 W; d) 25 V – 20 V – 25 V disturbances operating with an output load of 100 W.

C. *Set-point change transient response*

Fig. 17 shows the response to a 60 V step change applied in the voltage reference when the converter is in steady-state with a regulated output voltage of 400 V. This test has been applied in two different equilibrium points. The excitation produces a deviation in the output voltage below 45% with respect to the reference excitation and a settling time of approximately 70 ms in both cases. It is worth pointing out that this result reveals the trade-off between the robustness to external disturbances and the performance for set-point variations.

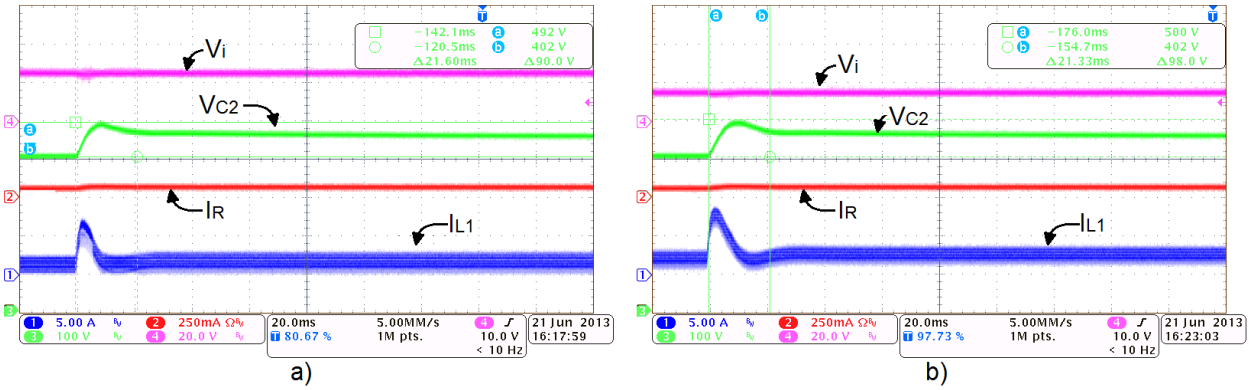

Fig. 17. Step response of the voltage regulator for a change from an equilibrium point (Output voltage, Input Voltage, Output Load) to another one by means of a change in the voltage reference: a) from (400 V, 25 V, 25 W) to (460 V, 25 V, 29 W) ; b) from (400 V, 15 V, 25 W) to (460 V, 15 V, 30 W)

D. *Frequency response*

In order to verify the frequency response prediction of the analytical study, frequency response measurements have been performed. Fig. 18 shows the experimental Nyquist curves for different equilibrium points covering the overall operating range of the converter. It can be observed that the Nyquist curves do not enter in the robustness region in any case. Slight differences with the simulated case can be noted due to the influence of the operational amplifiers bandwidth and the presence of parasitic elements in the circuit not considered in the simulation.

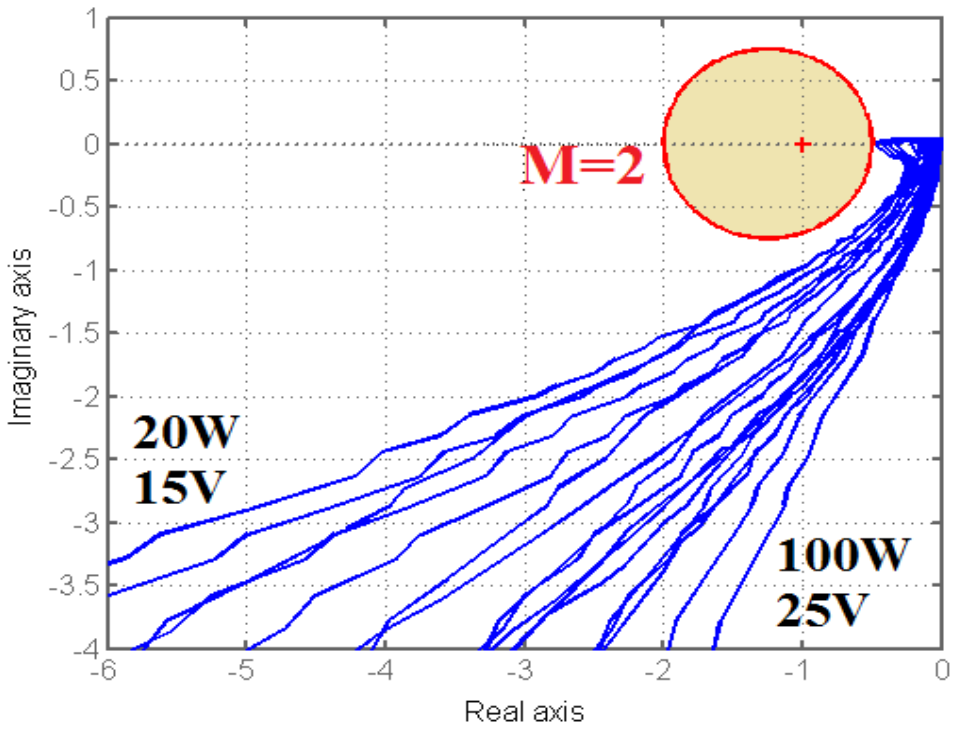

Fig. 18. Robustness regions for $M = 2$ compared with experimental results of the frequency response using a PI controller with $K_p = 0.0268$ and $K_i = 13.3$ cover the overall range of parameter variation.

VII. CONCLUSIONS

A complete description of a robust controller design obtaining output voltage regulation in a high DC-gain quadratic boost converter involving a sliding-mode current loop has been presented in this paper. The results show that this control scheme has a satisfactory performance regulating the output voltage in its overall operational range of output power and input voltage. The stability of the complete system has been treated as local by using the Routh-Hurwitz test constraining a stability region in the K_p - K_i plane which has been subsequently used as a reference to synthesize the PI compensator using the RLS-MIGO method. The stability and robustness of the overall system has been tackled by considering the possible variations in the output load or in the input voltage as parametric uncertainty. Several MATLAB simulations have been used to verify the theoretical approach and the converter expected performance when coping with important disturbances in the uncertain parameters. Moreover, experimental results using simple electronic circuits are in good agreement with the theoretical predictions and simulation results. The experiments have validated not only the high DC-gain capability of the quadratic boost converter operating with a hysteresis- based current controller but also the regulator robustness , ensured by the application of the loop shaping method in the PI synthesis.

It can be concluded that the RLS-MIGO method is compatible with the sliding-mode approach providing an efficient solution to synthesize the proposed two-loop controller for a high-order topology such as the quadratic boost converter. Future works with the same converter will be devoted to the study of its possible discontinuous and critical conduction modes together with the associated design of an appropriate controller.

APPENDIX

When $I_E(t)$ is constant (inner loop), the ideal sliding dynamics in (9) can be rewritten as

$$\begin{aligned} L2\frac{di_{L2}}{dt} &= v_{C1} - \frac{\overline{v_{C1}}^2 v_{C2}}{\overline{v_{C2}}\, v_{C1}} \\ C1\frac{dv_{C1}}{dt} &= -i_{L2} + \frac{\overline{i_{L2}}\,\overline{v_{C1}}}{v_{C1}} \\ RC2\frac{dv_{C2}}{dt} &= -v_{C2} + \frac{\overline{v_{C1}}\,\overline{v_{C2}}\, i_{L2}}{\overline{i_{L2}}\, v_{C1}} \end{aligned} \tag{a.1}$$

After some simple manipulations, (a.1) can be expressed as follows

$$\begin{aligned} L2\frac{di_{L2}}{dt} &= \left(1 + \frac{\overline{v_{C1}}}{v_{C1}}\right)(v_{C1} - \overline{v_{C1}}) - \frac{\overline{v_{C1}}^2}{\overline{v_{C2}}\, v_{C1}}(v_{C2} - \overline{v_{C2}}) \\ C1\frac{dv_{C1}}{dt} &= -(i_{L2} - \overline{i_{L2}}) - \frac{\overline{i_{L2}}}{v_{C1}}\,(v_{C1} - \overline{v_{C1}}) \\ RC2\frac{dv_{C2}}{dt} &= -(v_{C2} - \overline{v_{C2}}) + \frac{\overline{v_{C1}}\,\overline{v_{C2}}}{\overline{i_{L2}}\, v_{C1}}(i_{L2} - \overline{i_{L2}}) - \frac{\overline{v_{C2}}}{v_{C1}}(v_{C1} - \overline{v_{C1}}) \end{aligned} \tag{a.2}$$

Consider now the Lyapunov candidate function defined by

$$\boldsymbol{V}(i_{L2}, v_{C1}, v_{C2}) = \frac{1}{2}\left[L2\frac{\overline{v_{C2}}}{\overline{v_{C1}}}(i_{L2} - \overline{i_{L2}})^2 + C1\left(\frac{\overline{v_{C2}}}{\overline{v_{C1}}} + \frac{\overline{v_{C2}}}{v_{C1}}\right)(v_{C1} - \overline{v_{C1}})^2 + \frac{\overline{i_{L2}}}{\overline{v_{C2}}} R\, C2(v_{C2} - \overline{v_{C2}})^2\right] \tag{a.3}$$

Note that $V(i_{L2}, v_{C1}, v_{C2}) > 0, V(\overline{i_{L2}}, \overline{v_{C1}}, \overline{v_{C2}}) = 0$, and that this function is well defined because $v_{C1} > 0$ (see condition in (7)). The time derivative of $\boldsymbol{V}$ is given by

$$\begin{aligned}\dot{\boldsymbol{V}}(i_{L2}, v_{C1}, v_{C2}) = &\frac{\overline{v_{C2}}}{\overline{v_{C1}}}(i_{L2} - \overline{i_{L2}})L2\frac{di_{L2}}{dt} \\ &+ \left[\left(\frac{\overline{v_{C2}}}{\overline{v_{C1}}} + \frac{\overline{v_{C2}}}{v_{C1}}\right)(v_{C1} - \overline{v_{C1}}) - \frac{1}{2}\frac{\overline{v_{C2}}}{{v_{C1}}^2}(v_{C1} - \overline{v_{C1}})^2\right] C1\frac{dv_{C1}}{dt} \\ &+ \frac{\overline{i_{L2}}}{\overline{v_{C2}}}(v_{C2} - \overline{v_{C2}})R\ C2\frac{dv_{C2}}{dt}\end{aligned} \tag{a.4}$$

Developing each term of the previous expression leads to

$$\begin{aligned}\dot{\boldsymbol{V}}(i_{L2}, v_{C1}, v_{C2}) = &\frac{1}{2}\frac{\overline{v_{C2}}\, i_{L2}}{{v_{C1}}^2}(v_{C1} - \overline{v_{C1}})^2 - \frac{1}{2}\frac{\overline{i_{L2}}\,\overline{v_{C1}}\,\overline{v_{C2}}}{{v_{C1}}^3}(v_{C1} - \overline{v_{C1}})^2 \\ &- \frac{\overline{i_{L2}}}{v_{C1}}\left(\frac{\overline{v_{C2}}}{\overline{v_{C1}}} + \frac{\overline{v_{C2}}}{v_{C1}}\right)(v_{C1} - \overline{v_{C1}})^2 - \frac{\overline{i_{L2}}}{\overline{v_{C2}}}(v_{C2} - \overline{v_{C2}})^2 \\ &- \frac{\overline{i_{L2}}}{v_{C1}}(v_{C1} - \overline{v_{C1}})(v_{C2} - \overline{v_{C2}})\end{aligned} \tag{a.5}$$

But, $\overline{i_{L2}} > 0, \overline{v_{C1}} > 0, \overline{v_{C2}} > 0$ because of the nature of the power circuit, then, $-\frac{\overline{\mathrm{i_{L2}}}\,\overline{\mathrm{v_{C1}}}\,\overline{\mathrm{v_{C2}}}}{{\mathrm{v_{C1}}}^3}(\mathrm{v_{C1}} - \overline{\mathrm{v_{C1}}})^2 < 0$. Therefore,

$$\begin{aligned}\dot{\boldsymbol{V}}(i_{L2}, v_{C1}, v_{C2}) = &\frac{1}{2}\frac{\overline{v_{C2}}\, i_{L2}}{{v_{C1}}^2}(v_{C1} - \overline{v_{C1}})^2 - \frac{\overline{i_{L2}}}{v_{C1}}\left(\frac{\overline{v_{C2}}}{\overline{v_{C1}}} + \frac{\overline{v_{C2}}}{v_{C1}}\right)(v_{C1} - \overline{v_{C1}})^2 - \frac{\overline{i_{L2}}}{\overline{v_{C2}}}(v_{C2} - \overline{v_{C2}})^2 \\ &- \frac{\overline{i_{L2}}}{v_{C1}}(v_{C1} - \overline{v_{C1}})(v_{C2} - \overline{v_{C2}})\end{aligned} \tag{a.6}$$

If $\frac{1}{2}\mathrm{i_{L2}} < \overline{\mathrm{i_{L2}}}$ (i.e. $\mathrm{i_{L2}} < 2\overline{\mathrm{i_{L2}}}$), then

$$\dot{\boldsymbol{V}}(i_{L2}, v_{C1}, v_{C2}) = -\frac{\overline{i_{L2}}\,\overline{v_{C2}}}{v_{C1}\overline{v_{C1}}}(v_{C1} - \overline{v_{C1}})^2 - \frac{\overline{i_{L2}}}{\overline{v_{C2}}}(v_{C2} - \overline{v_{C2}})^2 - \frac{\overline{i_{L2}}}{v_{C1}}(v_{C1} - \overline{v_{C1}})(v_{C2} - \overline{v_{C2}}) \tag{a.7}$$

Expressing (a.7) in matrix form, namely, $\dot{\mathrm{V}} = \mathrm{x}'\mathrm{Q}\mathrm{x}$, results in

$$\dot{\boldsymbol{V}}(i_{L2}, v_{C1}, v_{C2}) = -\underbrace{\begin{bmatrix}(i_{L2} - \overline{i_{L2}}) & (v_{C1} - \overline{v_{C1}}) & (v_{C2} - \overline{v_{C2}})\end{bmatrix}}_{x'}\underbrace{\begin{bmatrix}0 & 0 & 0 \\ 0 & \frac{\overline{i_{L2}}\,\overline{v_{C2}}}{v_{C1}\overline{v_{C1}}} & \frac{\overline{i_{L2}}}{2v_{C1}} \\ 0 & \frac{\overline{i_{L2}}}{2v_{C1}} & \frac{\overline{i_{L2}}}{\overline{v_{C2}}}\end{bmatrix}}_{Q}\underbrace{\begin{bmatrix}i_{L2} - \overline{i_{L2}} \\ v_{C1} - \overline{v_{C1}} \\ v_{C2} - \overline{v_{C2}}\end{bmatrix}}_{x} \tag{a.8}$$

If $\left(\frac{\overline{\mathrm{i_{L2}}}\,\overline{\mathrm{v_{C2}}}}{\mathrm{v_{C1}}\overline{\mathrm{v_{C1}}}}\right)\frac{\overline{\mathrm{i_{L2}}}}{\overline{\mathrm{v_{C2}}}} - \frac{\overline{\mathrm{i_{L2}}}^2}{4{\mathrm{v_{C1}}}^2} = \frac{\overline{\mathrm{i_{L2}}}^2}{\mathrm{v_{C1}}}\left(\frac{1}{\overline{\mathrm{v_{C1}}}} - \frac{1}{4\mathrm{v_{C1}}}\right)$ is positive, then $\mathrm{Q} \geq 0$. This is true if $4\mathrm{v_{C1}} > \overline{\mathrm{v_{C1}}}$, i.e., $\mathrm{v_{C1}} > \frac{1}{4}\overline{\mathrm{v_{C1}}}$.

In conclusion, if the conditions $i_{L2} < 2\overline{i_{L2}}$ and $v_{C1} > \frac{1}{4}\overline{v_{C1}}$ are satisfied, then $\dot{V}(i_{L2}, v_{C1}, v_{C2}) \leq 0$. Moreover, $\dot{V}(i_{L2}, v_{C1}, v_{C2}) = 0$ for $v_{C1} = \overline{v_{C1}}$ and $v_{C2} = \overline{v_{C2}}$, which, considering the above conditions, implies $i_{L2} = \overline{i_{L2}}$, i_{L1} being equal to I_E. Then, $\dot{V}(i_{L2}, v_{C1}, v_{C2}) = 0$, only for the equilibrium point. Therefore, the system is asymptotically stable by the LaSalle's invariance principle [43]-[44].

REFERENCES

[1] F. Blaabjerg, Z. Chen and S.B. Kjaer, "Power electronics as efficient interface in dispersed power generation systems," *IEEE Trans. Power Electron.*, vol. 19, no. 5, pp. 1184-1194, Sept. 2004.

[2] Q. Li and P. Wolfs, "A review of the single phase photovoltaic module integrated converter topologies with three different DC link configurations," *IEEE Trans. Power Electron.*, vol. 3, no. 3, pp. 1320-1333, May. 2008.

[3] S. Lee, P. Kim and S. Choi, "High step-up soft-switched converters using voltage multiplier cells," *IEEE Trans. Power Electron.*, vol. 28, no. 7, pp. 3379-3387, Jul. 2013.

[4] A. Stupar, T. Friedli, J. Miniböck and J.W. Kolar, "Towards a 99% Efficient Three-Phase Buck-Type PFC Rectifier for 400-V DC Distribution Systems," *IEEE Trans. Power Electron.*, vol. 27, no. 4, pp. 1732-1744, Apr. 2012.

[5] Rockwell Automation, "Common DC bus: Selection guide," Publication DRIVES-SG001B-EN-P. Sep. 2005.

[6] F.H. Dupont, C. Rech, R. Gules and J.R. Pinheiro, "Reduced-order model and control approach for the boost converter with a voltage multiplier cell," *IEEE Trans. Power Electron.*, vol. 28, no. 7, pp. 3395-3404, Jul. 2013.

[7] G. Ramanjaneyulu and M. Subbarao, "Sliding mode current controller for transformer less DC-DC converter with high step-up voltage gain," in Proc. Int. Conf. on Advances in Electrical and Electronics Engineering (AEEE), Jul. 2012, pp. 1-8.

[8] M. Aamir and M.Y. Shinwari, "Design, implementation and experimental analysis of two-stage boost converter for grid connected photovoltaic system," in Proc. IEEE Int. Conf. on Computer Science and Information Technology (ICCSIT), Jul. 2010, pp. 194-199.

[9] K.C. Tseng, and T.J. Liang, "Novel high-efficiency step-up converter," *IEE Proc. Electric Power Appl.*, vol. 151, no.2, pp.182-190, Mar. 2004.

[10] F.S. Garcia, J.A. Pomilio, and G. Spiazzi, "Comparison of non-insulated, high-gain, high-power, step-up DC-DC converters," in 27th Annual IEEE Applied Power Electronics Conference and Exposition (APEC), Feb. 2012, pp. 1343-1347.

[11] M.G. Ortiz-Lopez, J. Leyva-Ramos, E.E. Carbajal-Gutierrez and J.A. Morales-Saldaña, "Modelling and analysis of switch-mode cascade converters with a single active switch," *IET Power Electron.*, vol. 1, no. 4, pp. 478-487, Dec. 2008.

[12] O. Lopez-Santos, L. Martinez-Salamero, G. Garcia, H. Valderrama-Blavi and D.O. Mercuri, "Efficiency analysis of a sliding-mode controlled quadratic boost converter," *IET Power Electron.*, vol. 6, no. 2, pp. 364-373, Feb. 2013.

[13] C. Olalla, R. Leyva, I. Queinnec and D. Maksimovic, "Robust Gain-Scheduled Control of Switched-Mode DC–DC Converters," *IEEE Trans. Power Electron.*, vol. 27, no. 6, pp. 3006-3019, Jun. 2012.

[14] C. Olalla, R. Leyva, A. El Aroudi, I. Queinnec and D. Maksimovic, "Robust LQR Control of PWM Converters: An LMI Approach," *IEEE Trans. Ind. Electron.*, vol. 56, no. 7, pp. 2548-2558, Jul. 2009.

[15] J. Linares-Flores, A. Hernandez Mendez, C. Garcia-Rodriguez, H. Sira-Ramirez, "Robust Nonlinear Adaptive Control of a "Boost" Converter via Algebraic Parameter Identification," *IEEE Trans. Ind. Electron.*, vol. 61, no. 8, pp. 4105-4114, Aug. 2014.

[16] F. Alonge, F. D'Ippolito, T. Cangemi, "Identification and Robust Control of DC/DC Converter Hammerstein Model," *IEEE Trans. Power Electron.*, vol. 23, no. 6, pp. 2990-3003, Nov. 2008.

[17] J. Leyva-Ramos, M.G. Ortiz-Lopez, L.H. Diaz-Saldierna and J.A. Morales-Sandaña, "Switching regulator using a quadratic boost converter for wide DC conversion ratios," *IET Power Electron.*, vol. 2, no. 5, pp. 605-613, Sep. 2009.

[18] J.A. Morales-Saldaña, R. Galarza-Quirino, J. Leyva-Ramos, E.E. Carbajal-Gutierrez and M.G. Ortiz-Lopez, "Multiloop controller design for a quadratic boost converter," *IET Elect. Power Appl.*, vol. 1, no. 3, pp. 362-367, May. 2007.

[19] J.A. Morales-Saldaña, R. Loera-Palomo, E. Palacios-Hernández, J.L. González-Martínez, "Modelling and control of a DC-DC quadratic boost converter with R2P2," *IET Power Electron.*, vol. 7, no. 1, pp. 11-,22, Jan. 2014.

[20] C.Y. Chan, "Analysis and experimental study of an output feedback controller for a high-order boost dc-dc converter," *IET Power Electron.*, vol. 6, no. 7, pp. 1279-1287, Aug. 2013.

[21] M. Hernandez-Gomez, R. Ortega, F. Lamnabhi-Lagarrigue, G. Escobar, "Adaptive PI Stabilization of Switched Power Converters," *IEEE Trans. Control Systems Technology*, vol. 18, no. 3, pp. 688-698, May. 2010

[22] J.A. Barrado, A. El Aroudi, H. Valderrama-Blavi, J. Calvente, and L. Martinez-Salamero, "Analysis of a Self-Oscillating Bidirectional DC–DC Converter in Battery Energy Storage Applications," *IEEE Trans. on Power Delivery*, vol. 27, no. 3, pp. 1292-1300, Jul. 2012.

[23] S.-C. Tan; Y.M. Lai and C.K. Tse, "General Design Issues of Sliding-Mode Controllers in DC–DC Converters," *IEEE Trans. Ind. Electron.*, vol. 55, no. 3, pp. 1160-1174, Mar. 2008.

[24] S-.C. Tan, Y.M. Lai, C-.K. Tse, L. Martinez-Salamero and C.K. Wu, "A fast-response sliding-mode controller for boost-type converters with a wide range of operating conditions," *IEEE Trans. Ind. Electron.*, vol. 54, no. 6, pp. 3276-3285, Dec. 2007.

[25] E. Vidal-Idiarte, C. Carrejo, J. Calvente and L. Martinez-Salamero, "Two-loop digital sliding mode control of DC-DC power converters based on predictive interpolation," *IEEE Trans. Ind. Electron.*, vol. 58, no. 6, pp. 2491-2500, Jun. 2011.

[26] Z. Chen, "PI and Sliding Mode Control of a Cuk Converter," IEEE Trans. Power Electron., vol. 27, no. 8, pp. 3695-3703, Aug. 2012.

[27] P.K. Singh, Y.V. Hote, M.M. Garg, "Comments on "PI and sliding mode control of a Cûk converter"," *IEEE Trans. Power Electron.*, vol. 29, no. 3, pp. 1551-1552, Mar. 2014.

[28] Z. Chen, W. Gao; J. Hu; X. Ye, "Closed-Loop Analysis and Cascade Control of a Nonminimum Phase Boost Converter," *IEEE Trans. Power Electron.*, vol. 26, no. 4, pp. 1237-1252, Apr. 2011.

[29] R.-J. Wai, L.-C. Shih, "Design of Voltage Tracking Control for DC–DC Boost Converter via Total Sliding-Mode Technique," *IEEE Trans. Ind. Electron.*, vol. 58, no. 6, pp. 2502-2511, Jun. 2011.

[30] H. Sira-Ramirez, "On the Generalized PI Sliding Mode Control of DC-to-DC Power Converters: A Tutorial," *Int. Journal of Control*, vol. 76, no. 9-10, pp. 1018-1033, 2003.

[31] O. López, L. García de Vicuña, M. Castilla, J. Matas and M. López, "Sliding-mode-control design of a high-power-factor buck-boost rectifier," *IEEE Trans. Ind. Electron.*, vol. 46, no. 3, pp. 604-612, Jun. 1999.

[32] J. Matas, L. García de Vicuña, J. Miret, J.M. Guerrero, and M. Castilla, "Feedback linearization of a single-phase active power filter via sliding mode control," *IEEE Trans. Ind. Electron.*, vol. 23, no. 1, pp. 116-125,Jan. 2008.

[33] D. Cortés, N. Vásquez, and J. Alvarez-Gallegos "Dynamic sliding-mode control of the boost inverter," *IEEE Trans. Ind. Electron.*, vol. 56, no. 9, pp. 3467-3476, Sep. 2009.

[34] L. Martinez-Salamero, G. Garcia, M. Orellana, C. Lahore and B. Estibals, "Start-up control and voltage regulation in a boost converter under sliding-mode operation," *IEEE Trans. Ind. Electron.*, vol. 60, no. 10, pp. 4637-4649, Oct. 2013.

[35] H. Panagopoulos and K. Astrom, "PID Control Design and H_∞ Loop Shaping," in Proc. Int. Conf. on Control Appl., Aug. 1999. pp. 103-108.

[36] H. Panagopoulus, K.J. Astrom and T. Hagglund, "Design of PID controllers based on constrained optimisation," *IEE Proc. on Control Theory Appl.*, vol. 149, no. 1, pp. 32-40, 2002.

[37] K.J. Astrom, T. Hagglund. "Revisiting the Ziegler-Nichols step response method for PID control," *Journal of Process Control*., vol. 14, pp. 635-650, 2004.

[38] K.J. Aström, H. Panagopoulus, T. Hägglund. “Design of PI controllers based on Non-Convex Optimization," *Automatica*., vol. 34, no. 5, pp. 585-601, 1998.
[39] R.W. Erickson, and D. Maksimovic, Fundamentals of power electronics, 2th. Edition. Massachussetts: Kluwer Academic Publishers, 2000.
[40] H. Sira-Ramirez and R. Silva-Ortigoza, Control Design Techniques in Power Electronic Devices, 1th. Edition. Germany: Springer, 2006.
[41] V.I. Utkin, J. Guldner and J. Shi, Sliding mode control in electromechanical systems, CRC Press, 2th. Edition, Taylor and Francis Group, 2009.
[42] F. Golnaraghi and B.C. Kuo, Automatic Control Systems, 9th Edition USA: John Wiley and Sons, 2010.
[43] H.K. Khalil, Nonlinear Systems, London:MacMillan, 1992.
[44] J.P. LaSalle, “The stability of Dynamical Systems,” In proc. of the Regional Conference Series in Applied Mathematics, vol. 25, 1976.